Chemical Engineering Journal 490 (2024) 151594

Contents lists available at ScienceDirect

Chemical Engineering Journal

journal homepage: www.elsevier.com/locate/cej

# Ultrafast In-Situ synthesis of flexible $MoO_3$ anode in five seconds for High-Performance aqueous zinc ion hybrid capacitor

Penghao Chai [a], Yuchen Li [a], Qiulong Guan [a], Jianghuan Li [a], Lijie Li [b], Lixia Bao [c], Jiong Peng [a,*], Xin Li [a,*]

[a] School of Chemistry and Chemical Engineering, Beijing Institute of Technology, Beijing 100081, China
[b] School of Material Science and Engineering, Beijing Institute of Technology, Beijing 100081, China
[c] Analysis & Testing Center, Beijing Institute of Technology, Beijing 100081, China

ARTICLE INFO

*Keywords:*
Ultrafast synthesis
Aqueous zinc-ion capacitors
Microwave carbonthermal shock
$MoO_3$ anode

ABSTRACT

The efficient synthesis of high-performance α-$MoO_3$ on flexible conductive substrates is crucial for enhancing its value in the field of energy storage. However, traditional synthesis methods currently employed often suffer from slow heating rates, intricate reaction processes involving multiple steps, sluggish reaction kinetics, high energy consumption, and prolonged preparation times, thereby hindering efficient production. Presented herein is a facile, ultrafast, and versatile approach utilizing microwave carbon thermal shock, a one-step reaction synthesis of α-$MoO_3$ on carbon substrates within 5 s. During microwave carbon thermal shock, the precursor salt experiences an extremely rapid heating rate, swiftly decomposing to form small-sized α-$MoO_3$ crystals. Simultaneously, this process promotes the oxidation of adjacent carbon sites, thereby imparting multi-scale defects and oxygen-containing functional groups to the resulting carbon cloth (CC). The exceptionally low reaction energy barriers and superior Gibbs free energy (ΔG) further substantiate the advantages of the microwave carbon thermal shock strategy over traditional synthesis methods in terms of both kinetics and thermodynamics. The air-assisted transient microwave carbonthermal shock (AMCTS) process circumvents high energy requirements, multistep reactions, and extended preparation times, endowing AMCTS-CC@$MoO_3$ with remarkable flexibility and processability. In demonstrating its practical utility within zinc-ion hybrid micro capacitors, it exhibits outstanding specific capacitance (up to 2300mF $cm^{-2}$) and mechanical stability. This air-assisted transient microwave thermal shock process provides an efficient route for ultrafast and low-cost synthesis of flexible zinc-ion anode materials.

## 1. Introduction

Today, the world faces numerous energy challenges, necessitating the development of efficient electrochemical energy storage technologies. Lithium-ion batteries (LIBs) are pivotal in modern energy systems owing to their high energy density, extended cycle life, and excellent cycling performance [1,2]. However, safety concerns and the scarcity of lithium resources significantly impede the widespread utilization of LIBs. Therefore, it is imperative to explore new energy storage technologies that offer secure, environmentally friendly, and cost-effective alternatives. As an emerging energy storage device, the aqueous zinc ion hybrid capacitor (ZIC) seamlessly integrates the exceptional performance, non-toxicity, and high safety of zinc ion batteries (ZIBs) and supercapacitors (SCs). This combination positions it as a frontrunner among promising energy storage systems, showcasing remarkable potential in the realm of energy storage technology [3–6]. The anode's role in practical ZIC application is paramount, influencing both energy density and cost [7,8]. Due to its high theoretical capacity (820 mAh $g^{-1}$) and cost competitiveness, metallic zinc is widely regarded as the most prevalent negative electrode material in Zn-ion hybrid capacitors (ZIHCs)[9,10]. However, practical zinc metal anode utilization faces various limitations. Firstly, compensating for its low utilization rate necessitates an excess of zinc anode, resulting in high negative-to-positive electrode (N/P) ratios reaching several tens or even hundreds, thus diminishing the actual energy density of the energy storage device. Secondly, zinc dendrite growth and complex side reactions commonly lead to reduced Coulombic efficiency, worsened reversibility, severe capacity degradation, and potentially short circuits in ZIHCs. Despite

* Corresponding author.
*E-mail addresses:* jiongpeng@163.com (J. Peng), klkxlx@163.com (X. Li).

https://doi.org/10.1016/j.cej.2024.151594
Received 28 February 2024; Received in revised form 18 April 2024; Accepted 22 April 2024
Available online 23 April 2024

efforts to mitigate zinc dendrite growth and side reactions through anode modification or electrolyte design, satisfactory performance remains elusive [11]. Molybdenum trioxide ($MoO_3$) as a pseudocapacitor material has attracted great interest from researchers for its cost-effectiveness, non-toxicity, superior electrochemical activity, and stability [12–14]. Among various types of $MoO_3$, including the orthorhombic phase α-$MoO_3$, the monoclinic phase β-$MoO_3$, and the hexagonal phase h-$MoO_3$. $MoO_3$ is an attractive material that has been reported in energy storage devices as battery anodes. Recently, orthorhombic $MoO_3$ (α-$MoO_3$) has been investigated for ZIB applications. The discharge potential was found to be ca. 0.5 V vs. $Zn^{2+}$/Zn, which makes $MoO_3$ promising for ZIB intercalation anodes [15,16]. The robust layered orthorhombic structure of α-$MoO_3$ allows rapid ion intercalation and deintercalation between its layers without structural collapse, making it widely studied [17–19]. The paramount attributes of $MoO_3$ lie in its potential range available for anodes and its exceptionally high theoretical capacity, reaching up to 1005C $g^{-1}$. These features hold promise for enabling the coexistence of high energy density as well as high power density in ZICs. Nevertheless, the inherent challenge lies in its intrinsic conductivity, hindering rapid electron transfer within the electrode [20,21]. To mitigate this concern, a widely adopted and efficient strategy entails the in-situ growth of $MoO_3$ on conductive substrates, such as carbon nanotubes and carbon cloth [22,23]. This approach not only establishes a 3D conductive network to enhance electron transport but also facilitates better contact between electrode and electrolyte.

Up to the present, the most prevalent approaches for fabricating $MoO_3$ on conductive substrates primarily encompass hydrothermal synthesis [24–26], electrochemical deposition [27,28], and vapor-phase deposition synthesis [29,30]. Specifically, hydrothermal synthesis is commonly acknowledged as a straightforward and feasible approach to attain $MoO_3$ on conductive substrates. However, due to kinetic limitations, it typically necessitates several hours of reaction and must be carried out at high temperatures and pressure [31], making it overly demanding and hazardous for industrial manufacturing. In contrast, electrochemical deposition offers a time-efficient (mere minutes), cost-effective, and facile approach for synthesizing $MoO_3$. Nonetheless, it still suffers from issues such as uneven coating due to inevitable concentration polarization, as well as uncontrolled nucleation and growth, resulting in poor crystallinity of the target phase. Physical vapor deposition (PVD) emerges as a standout technique among vapor-phase deposition methods, known for its proficiency in fabricating $MoO_3$ films with superior crystalline quality and precise modulation. However, this method generally demands a substantial amount of energy for vaporizing the source material. On the other hand, chemical vapor deposition (CVD) requires significantly less energy for precursor sublimation compared to PVD. Nevertheless, the toxic nature of molybdenum hexacarbonyl ($Mo(CO)_6$), the primary precursor utilized in the CVD process, severely restricts its widespread application [32]. In conclusion, it is imperative for industrial production to explore and develop a straightforward, time-efficient, and efficient large-scale approach for acquiring high-quality and well-structured $MoO_3$ on conductive substrates.

Herein, we report an air-assisted transient microwave carbon thermal shock technique for the in situ synthesis of α-$MoO_3$ on conductive carbon cloth (CC). In this procedure, the conductive carbon cloth absorbs microwaves to induce carbon thermal shock that propels the prompt decomposition of the preloaded precursor $(NH_4)_2MoO_4$, which results in the rapid in situ growth of α-$MoO_3$ on the substrate. In parallel, the rapid surface modification of carbon cloth was achieved through the synergistic interplay of catalyzed etching with α-$MoO_3$ and accelerated functionalization by oxygen-containing functional groups in the air atmosphere. The entire treatment process spans less than 5 s, circumventing the utilization of strong oxidants and harmful chemicals, exhibiting high efficiency, safety, and environmental benignity. In contrast to traditional synthesis methods like hydrothermal processes necessitating prolonged heating to produce intermediate metastable h-$MoO_3$ phase before obtaining α-$MoO_3$, microwave carbonthermal shock facilitates a one-step synthesis of stable phase α-$MoO_3$ within seconds. As anticipated, a flexible anode based on α-$MoO_3$ with outstanding electrochemical performance has been constructed. Within the potential window range of −0.8 to 0.1 V, the areal capacitance of AMCTS-CC@$MoO_3$ can reach 2300 mF $cm^{-2}$ under the areal current density of 1 mA $cm^2$. Moreover, with its remarkable mechanical stability and processability, AMCTS-CC@$MoO_3$ serves as a facile choice for the anode in constructing a flexible quasi-solid-state zinc ion hybrid capacitor, incorporating CC@nitrogen-doped hierarchal porous carbon (CC@N-HPC) as the cathode and Polyacrylamide-$ZnSO_4$ (PAM-$ZnSO_4$) as the electrolyte. The microdevice boasts a substantial areal capacity of 800 mF $cm^{-2}$ at 1 mA $cm^{-2}$, a commendable areal energy density of 321 μWh $cm^{-2}$, along with a notable power density of 8 mW $cm^{-2}$, it also showcases excellent cycling stability, retaining 90 % of its capacity after 10,000 cycles. Additionally, the ZIC is remarkably flexible, retaining its capacity even when bent at arbitrary angles, showcasing its potential for application in wearable electronic devices. This study may pave the way for a novel and ultrafast synthesis approach for metal oxide-based anode materials at a low cost.

## 2. Results and discussion

As reported, carbon materials serve as excellent microwave receptors, enabling coupling with microwave radiation and resulting in ultrafast heating [33,34]. Simultaneously, relevant studies indicate that carbon materials can undergo catalytic etching facilitated by metal or metal oxide particles at high temperatures [35]. By leveraging these dual attributes, the synthesis of α-$MoO_3$ on carbon cloth was conducted through the air-assisted transient microwave carbon thermal shock method illustrated in Fig. 1a. In a typical experiment, the aqueous solution of $(NH_4)_2MoO_4$ is utilized to immerse the original carbon cloth (CC), which is subsequently dried to fabricate the CC@$(NH_4)_2MoO_4$ precursor. Subsequently, it undergoes carbon thermal shock in a household microwave oven filled with air. Upon exposure to microwaves, the carbon cloth (CC) interacted with microwave energy, inducing a rapid carbothermal shock that swiftly increased the temperature and emitted intense light. the $(NH_4)_2MoO_4$ precursor decomposed to yield α-$MoO_3$ as the temperature continued to rise [36]. In this procedure, the oxygen atoms in proximity to the α-$MoO_3$ nanoparticles underwent in situ oxidation of nearby carbon species. Concurrently, the abundant oxygen provided by the atmosphere supports a sustained and controlled oxidation reaction of carbon. This process results in the construction of a flexible anode, characterized by a carbon cloth with multiscale defects and oxygen-containing functional groups. Additionally, the anode exhibited uniform encapsulation of small-sized α-$MoO_3$ nanoparticles.

Characterization via scanning electron microscopy (SEM) was employed to analyze the morphological and structural changes of the samples obtained, both before and after exposure to thermal shock. Unlike the original CC, which exhibits a smooth and hydrophobic surface (Fig. 1b), the carbon cloth subjected to thermal shock (with no precursor loading) becomes rougher with numerous defect pores, indicating uniform surface modification of CC (Fig. S1). Prior to carbon thermal shock, the $(NH_4)_2MoO_4$ precursor primarily accumulates in the gaps between carbon fibers (Fig. 1c), resulting in a substantial exposure of the carbon fiber surface. Given the brief duration of the carbon thermal shock (i.e., 5 s), the integrity of the fabric structure and individual fibers is well preserved (Fig. 1d). Alternatively, when the thermal shock persists for 10 s, it results in the carbon fibers being excessively oxidized, significantly deteriorating their structural coherence and integrity, as illustrated in Fig. S2. Simultaneously, the $(NH_4)_2MoO_4$ precursor experiences swift decomposition and subsequent redispersion due to the ultrafast thermal shock, resulting in the uniform coating of α-$MoO_3$ onto the carbon fibers, which was verified through energy

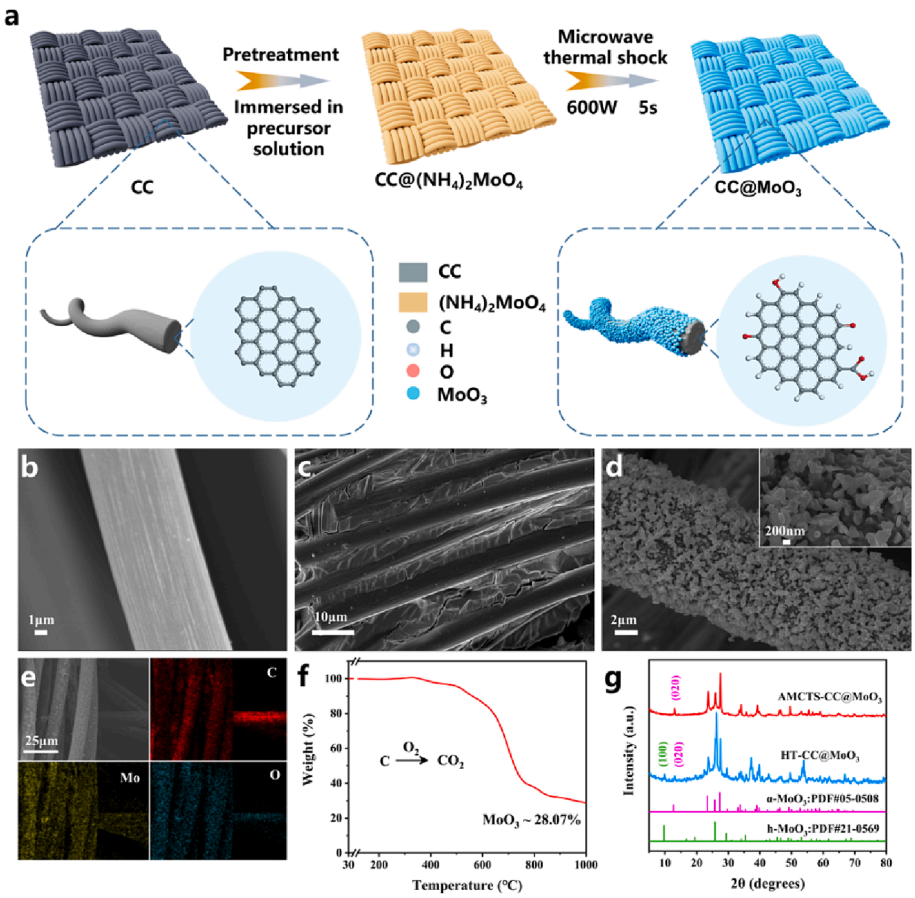


**Fig. 1.** a) A schematic representation illustrating the synthesis of AMCTS-CC@$MoO_3$ using air-assisted transient microwave carbon thermal shock (AMCTS). b-d) SEM images of original CC, CC@$(NH_4)_2MoO_4$ and AMCTS-CC@$MoO_3$ (Inset: high-resolution SEM of AMCTS-CC@$MoO_3$). e) Element mapping of AMCTS-CC@$MoO_3$. f) TGA curve of AMCTS-CC@$MoO_3$ from 30 to 1000 ℃, under air atmosphere. g) XRD patterns of the precursor of AMCTS-CC@$MoO_3$ and HT-CC@$MoO_3$.

dispersive X-ray spectroscopy (Fig. 1e). High-resolution SEM image clearly depicts the varied shape of α-$MoO_3$ nanoparticles, which range in size from 50 to 200 nm (Fig. S3), with observable crystal morphology (Fig. 1d, inset). Small particle formation is associated with the microwave carbon thermal shock process [37], wherein the ultra-high heating rates induce reactions with exceptionally fast reaction kinetics. In order to provide a comparative analysis with traditional synthesis routes, we opted for the representative hydrothermal method to prepare HT-CC@$MoO_3$. Samples obtained through hydrothermal methods typically exhibit uneven nucleation and a structure formed by the stacking of nanoplates, leading to a reduction in ion migration pathways (Fig. S4). The presence of smaller particle sizes through the thermal shock strategy contributes significantly to achieving enhanced electrochemical performance, characterized by enhanced rate capability and exceptional cyclic stability [38]. The $MoO_3$ content, measured through thermogravimetric analysis (TGA), is approximately 28.07 % (Fig. 1f).

Utilizing X-ray Diffraction (XRD), the compositional evolution during microwave carbon thermal shock and hydrothermal processes was monitored. Fig. 1g elucidates the dynamic evolution of XRD spectra for precursors and products in both microwave carbon thermal shock and hydrothermal reaction processes. In the XRD pattern of HT-CC@$MoO_3$ obtained from the hydrothermal reaction, distinctive peaks corresponding to the stable phase α-$MoO_3$, notably the (020), (110), (040), (021), (111) planes [39]. Furthermore, characteristic peaks indicative of the metastable intermediate phase h-$MoO_3$, such as the (100) plane [40], are observed, providing conclusive evidence that $(NH_4)_2MoO_4$ initially generates the intermediate phase h-$MoO_3$ during the hydrothermal reaction, subsequently transforming into the stable phase α-$MoO_3$. This observation aligns seamlessly with pertinent literature [41,42]. Conversely, the XRD pattern of CC@$MoO_3$ synthesized via microwave carbon thermal shock exclusively reveals peaks corresponding to the α-$MoO_3$ phase. Therefore, microwave carbon thermal shock synthesis allows for a one-step reaction to form flexible anode materials. The disparity in the synthesis mechanisms between microwave carbon thermal shock and traditional methods is attributed to their differing reaction kinetics. Methods conventionally employed, characterized by low heating rates, result in sluggish reaction kinetics as well as entail multi-step procedures. Conversely, the microwave carbon thermal shock approach involves ultra-high heating rates and one-step reaction processes, circumventing low-temperature reactions. This facilitates rapid reaction kinetics, holding the promise of swiftly constructing designed anode materials via a one-step reaction.

Fourier transform infrared spectroscopy (FT-IR), Raman spectroscopy, and X-ray photoelectron spectroscopy (XPS) analyses were employed for additional characterization of the composition and defect level of AMCTS-CC@$MoO_3$. As shown in Fig. 2a, a comparative analysis was performed on the FT-IR spectra of untreated CC between AMCTS-CC@$MoO_3$ samples reveals the generation of > COH, >C = O, and –COOH functional groups on the surface of CC following microwave carbon thermal shock. The defect levels of CC were examined using Raman spectroscopy before and after microwave carbon thermal shock. In Fig. 2b, it is evident that both samples displayed two distinct peaks at 1350 and 1580 $cm^{-1}$, indicative of the D-band and G-band of carbon materials [43,44]. According to the Raman spectra, the $I_D/I_G$ ratio, calculated for the AMCTS-CC@$MoO_3$, was 0.97, significantly surpassing the ratio observed in the original CC (0.69), signifying a considerable increase in defect content. Fig. 2c-e depicts the X-ray photoelectron spectroscopy (XPS) spectra of CC and AMCTS-CC@$MoO_3$, revealing

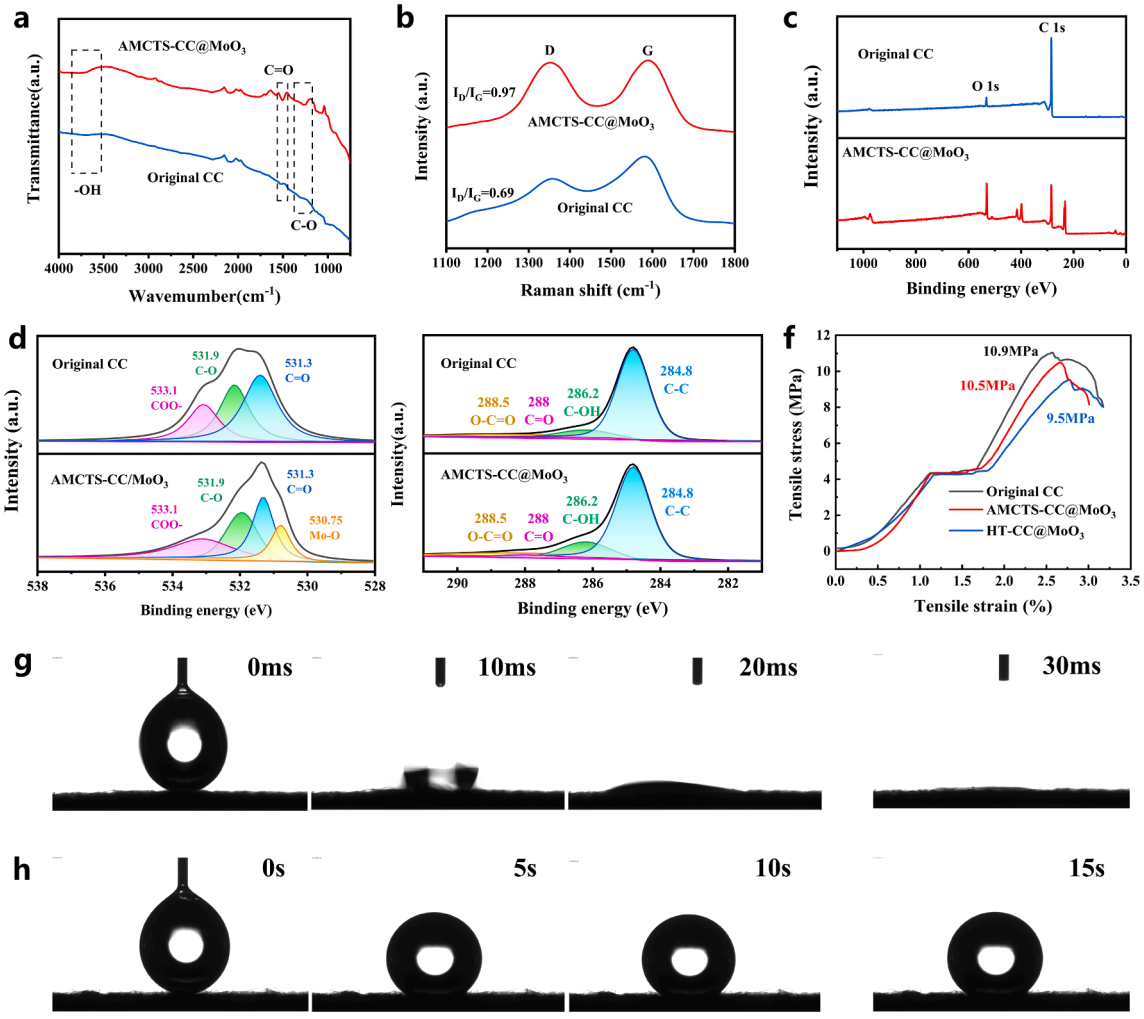


**Fig. 2.** Characterization of the original CC and AMCTS-CC@$MoO_3$ after carbon thermal shock. a) FT-IR spectra. b) Raman spectra. c)XPS spectra. High-resolution XPS spectra of d) C 1 s and e) O 1 s. f) Tensile stress–strain curves of original CC and AMCTS-CC@$MoO_3$ and HT-CC@$MoO_3$. g-h) The photo images of the wetting behavior of the original CC and AMCTS-CC@$MoO_3$ and HT-CC@$MoO_3$.

changes in surface chemical composition after microwave carbon thermal shock. At 284.8 and 532.6 eV, both curves display peaks attributed to C 1 s and O 1 s, respectively, whereas Mo 3p and Mo 3d peaks (Fig. S5) are only present in AMCTS-CC@$MoO_3$ [45]. Following microwave thermal shock, the ratio of C/O intensity in AMCTS-CC@$MoO_3$ is markedly reduced compared to that in the initial CC (Fig. 2c), suggesting the presence of oxygen-containing functional groups on the surface. Utilizing high-resolution XPS spectra, further investigation was conducted on the bonding states of C and O elements. The C 1 s peaks of both samples can be deconvoluted into four peaks corresponding to C-C (284.8 eV), C-OH (286.2 eV), C = O (288 eV), and O-C = O (288.5 eV) functional groups(Fig. 2d) [46]. After microwave carbon thermal shock, the C-$C_{sp2}$/O-C = O ratio in AMCTS-CC@$MoO_3$ decreased from 25.5 to 13.0, suggesting a higher degree of carbon oxidation. Three distinct peaks are observed in the O 1 s spectrum of the original CC, corresponding to oxygen in carboxyl groups (COO–, 533.1 eV), carbonyl groups (C = O, 531.3 eV), and oxygen single bonds in esters and carboxyl groups (O-C, 531.9 eV) (Fig. 2e) [46]. The clear increase in oxygen bond content in the AMCTS-CC@$MoO_3$ spectrum further supports the enrichment of oxygen-containing functional groups. Apart from these peaks, there is an observable occurrence of a metal–oxygen bond (Mo-O, 530.75 eV) specific to AMCTS-CC@$MoO_3$, providing further confirmation of the successful synthesis of α-$MoO_3$. Despite the introduction of defects, AMCTS-CC@$MoO_3$ maintains a tensile strength of 10.5 MPa (Fig. 2f), indicative of robust structural stability (Fig. S6).

The wettability of AMCTS-CC@$MoO_3$ experiences significant improvement due to the elevated levels of defects and oxygen-containing functional groups. The dynamic wetting process observation reveals that water droplets exhibit rapid infiltration into AMCTS-CC@$MoO_3$, completing the process within 30 ms. In contrast, even after 15 s, droplets on the untreated CC surface remain unchanged, exhibiting no apparent wetting (Fig. 2g-h). To demonstrate the enhanced ion-accessible surface area of AMCTS-CC@$MoO_3$ samples, dye absorption studies were conducted on untreated CC and AMCTS-CC@$MoO_3$ samples (Fig. S7). The specimens were submerged in a continuously stirred aqueous solution containing 5 mg $L^{-1}$ of methylene blue (MB) for a duration of 12 h. The MB solution containing AMCTS-CC@$MoO_3$ appears nearly colorless, while the solution containing untreated CC retains its blue color, similar to the original MB solution, suggesting considerable adsorption of dye molecules onto the AMCTS-CC@$MoO_3$ sample. UV–visible absorption spectra reveal a substantial reduction in MB intensity by AMCTS-CC@$MoO_3$ (with a peak at 665 nm) compared to untreated CC, indicating the increased absorption of MB dye molecules by AMCTS-CC@$MoO_3$ and confirming the enhanced ion-accessible surface area of AMCTS-CC@$MoO_3$ samples. Hence, employing the microwave carbon thermal shock route substantially amplifies the defect density and oxygen-containing functional groups within the CC, coupled with notable improvement in wetting and ion-accessible surface area. These advantages are poised to facilitate the realization of high electrochemical performance [47].

Contrary to traditional synthesis methods which necessitate prolonged heat treatments and involve complex multistep reactions, AMCTS facilitates a one-step reaction, achieving the synthesis of α-$MoO_3$ in just a few seconds (Fig. 3a). To gain deeper insights into the mechanistic disparities between $MoO_3$ formation in microwave carbon thermal shock and traditional synthesis routes, we employed first-principles calculations. The Gibbs free energy (ΔG) of the reactants and products involved in the structural transition process was analyzed using model structures at different temperatures. In traditional hydrothermal synthesis, a two-step reaction process is involved. During the initial step, the precursor first converts to the intermediate phase h-$MoO_3$. During this process, there is a transition in ΔG from positive to negative with increasing temperature, and the critical temperature ($T_c$) is evident in Step 1, indicating that once the temperature reaches $T_c$, the reaction irreversibly takes place [40]. Given the slow heating rate of the traditional synthesis path, it takes a considerable amount of time to reach Tc and form h-$MoO_3$. In Step 2, ΔG also exhibits a trend of becoming negative with increasing temperature (Fig. 3b). Unlike traditional methods, within the microwave carbon thermal shock process, the value of ΔG remains consistently negative, suggesting the perpetual spontaneity of the reaction (Fig. 3c). The rapid heating triggered ultrafast kinetics during the spontaneous process enable the precursor to undergo direct conversion to α-$MoO_3$ in a short time, without any intermediate reactions. This finding aligns with the conclusions drawn from XRD in the above experimental results.

Due to the ultrafast synthesis rate, high quality crystalline phase, and larger exposed surface area of accessible ions achieved by microwave carbothermal shock, these advantages make AMCTS-CC@$MoO_3$ a promising electrode material with great potential for practical applications in anode materials. Continuing with the electrochemical measurements using a three-electrode system to confirm the prepared negative electrode's capability as a high-performance Zn-ion capacitor (ZIC). The initial capacitance of CC itself can be negligibly disregarded. After microwave carbon thermal shock treatment, CC fibers exhibit a marginal increase in capacitance (Fig. S8). This phenomenon can be attributed to the microwave carbon thermal shock in an air atmosphere, inducing the generation of abundant hydrophilic functional groups (–COOH, –OH) on the surface of CC and expanding the ion-accessible surface area of CC fibers. Consequently, during the charge and discharge processes, CC manifests both pseudocapacitive and double-layer characteristics.

Fig. 4a and Fig. 4b provide additional evidence supporting the formation of high-performance $MoO_3$ on the carbon cloth surface following microwave carbonthermal shock treatment. Thanks to the aforementioned advantages, the CC fibers loaded with α-$MoO_3$ as electrodes demonstrate exceptionally high area-specific capacitance, reaching 2300 mF $cm^{-2}$ at the areal current density of 1 mA $cm^{-2}$ (Fig. 4b). AMCTS-CC@$MoO_3$ exhibits minimal curve distortion at increased scan rates (Fig. 4c), indicating an improved capacitance response and highlighting the significant enhancement in charge storage capacity through microwave-induced surface engineering. Fig. 4d depicts the GCD curves at different current densities, all exhibiting nearly symmetrical triangular shapes with identical charge and discharge times, and a Coulombic efficiency close to 100 %. This indicates excellent electrochemical reversibility. Additionally, there is no significant voltage drop observed in the GCD curves, suggesting that the overall resistance is low. Fig. 4e illustrates the rate performance of the AMCTS-CC@$MoO_3$ anode as the current density increases from 1 mA $cm^{-2}$ to 10 mA $cm^{-2}$. Due to the formation of a finely crystalline structure with ultrafine particle sizes through microwave thermal shock treatment, the AMCTS-CC@$MoO_3$

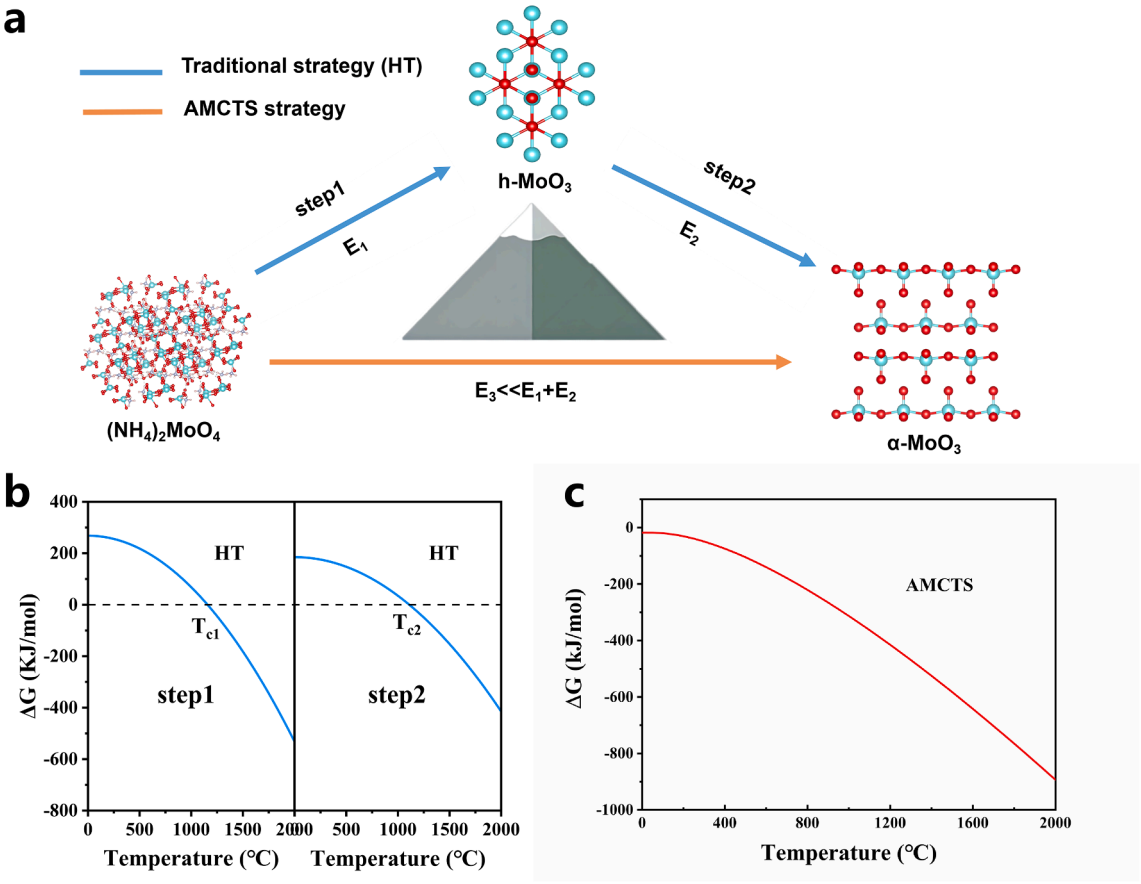


**Fig. 3.** a) Comparison of the reaction paths of the AMCTS and HT synthesis methods. b) ΔG of the reaction at different temperatures in the HT process. c) ΔG of the reaction at different temperatures in the AMCTS process.

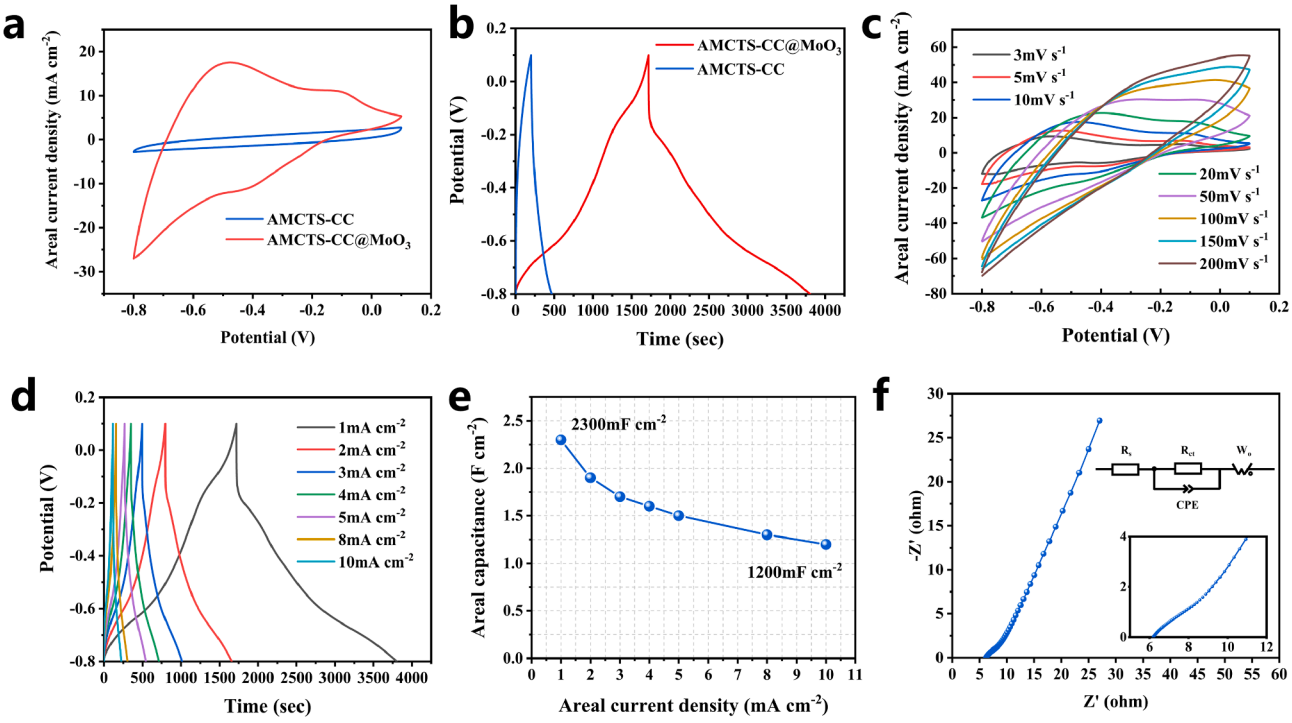


**Fig. 4.** Electrochemical performance of the CC and AMCTS-CC@$MoO_3$. a) CV curves and b) GCD curves. c) CV curves of AMCTS-CC@$MoO_3$ at scan rates ranging from 1 to 200 mV $s^{-1}$; (d) GCD curves of AMCTS-CC@$MoO_3$ at current densities from 1 to 10 mA $cm^{-2}$; (e) Rate performance of AMCTS-CC@$MoO_3$ as the current density increases from 1 A $cm^{-2}$ to 10 A $cm^{-2}$; (f) Nyquist plot of AMCTS-CC@$MoO_3$ (Inset: the equivalent circuit and the low-frequency impedance of AMCTS-CC@$MoO_3$).

exhibits excellent cyclic stability and outstanding rate performance. Even at an increased current density of 10 mA $cm^{-2}$, it maintains a remarkable rate capability of 1200 mF $cm^{-2}$. Furthermore, after 1000 cycles, the capacity retention rate remains at 80 % (Fig. S9). These performances surpass those achieved by electrodes prepared through hydrothermal methods. This indicates prominently that the electrode possesses outstanding stability and robust cycling performance, owing to its unique microstructure induced by microwave carbon thermal shock treatment. The Nyquist plot of AMCTS-CC@$MoO_3$ depicted in Fig. 4f, is accompanied by the respective equivalent circuit the low-frequency impedance of AMCTS-CC@$MoO_3$ outlined in the inset. Analysis through electrochemical impedance spectroscopy (EIS) unveils a Nyquist plot featuring a limited semicircle (Rct = 14.6 Ω, Rs = 3.8 Ω) and a linear component, indicating swift electron transfer and a high ion diffusion coefficient in the device. This suggests that the device possesses efficient charge transport and ion diffusion capabilities. For the assessment of its viability as a positive electrode material for zinc ion batteries, the Zn//AMCTS-CC@$MoO_3$ battery was assembled and tested (Fig. S10). It is obvious that the AMCTS-CC@MoO3 cathode is capable of achieving a high areal specific capacity of approximately 1124.6 mAh cm-2 at 0.1 mA $cm^{-2}$. These findings suggest that the microwave carbon thermal shock process is a viable strategy for producing high electrochemical performance anode materials.

Notably, the increased attention towards on-chip micro-power sources, like micro batteries and micro-supercapacitors, is a result of their high energy density and practical integration potential into miniaturized devices. This holds great promise for propelling the advancement of smart medical devices, artificial intelligence robots, and other self-powered micro-systems [48–50]. Based on the prepared AMCTS-CC@$MoO_3$, remarkable electrochemical performance, mechanical stability, flexibility, and processability have been demonstrated. The material offers flexibility in being cut into different patterns according to requirements (Fig. S11). The anode exhibits exceptional flexibility, allowing for bending and rotation (Fig. S12). As illustrated in Fig. 5a, a Zn-ion microcapacitor (ZIMC) based on the interdigitated AMCTS-CC@$MoO_3$ micro-electrode, CC@N-HPC electrode, and PAM-2 M $ZnSO_4$ gel electrolyte has been constructed. The electrochemical characteristics of the ZIC are further evaluated through CV and GCD curves. The CV curves of the AMCTS-CC@$MoO_3$ and CC@N-HPC electrodes (at a scan rate of 10 mV s-1) displayed in Fig. 5b show voltage windows for AMCTS-CC@$MoO_3$ between −0.8 and 0.1 V, and for CC@N-HPC between 0 and 0.9 V. The preparation of N-HPC was carried out according to our earlier research efforts, with comprehensive synthesis details provided in the experimental section of the supporting information. The electrochemical performance of CC@N-HPC is displayed in Fig. S13. As a result, the operating potential window for the ZIMC is within the range of 0 to 1.7 V. CV curves depicted in Fig. 5c across varying potential windows reveal a pronounced surge in current nearing 1.8 V, possibly due to electrolyte or water decomposition. Thus, the voltage window is capped at 0 to 1.7 V. Fig. 5d depicts CV curves at different scan rates from 3 to 100 mV $s^{-1}$, while Fig. 5e shows GCD curves at different scan rates from 1 to 10 mA $cm^{-2}$. The charge–discharge curves exhibit similarity and symmetry across all current densities, pointing to robust charge–discharge capabilities and low IR drop. The maximum areal specific capacitance reaches 800 mF $cm^{-2}$ at 1 mA $cm^{-2}$. Fig. 5f illustrates the Ragone plot of the assembled ZIMC, demonstrating a high areal energy density of 321 μWh $cm^{-2}$ at a power density of 1.1 mW $cm^{-2}$, surpassing recently reported flexible systems containing zinc-ion batteries and capacitors (Table S1). Fig. 5g exhibits the cycling performance of the flexible microdevice, maintaining a high level of capacity retention, reaching 90 % after 10,000 cycles at 20 mA $cm^{-2}$. The application of the device in powering a clock is demonstrated in Fig. 5h, showcasing its practical utility. Our investigation emphasizes the exceptional potential of AMCTS-CC@$MoO_3$, prepared through microwave carbon thermal shock, as an anode for high energy density capacitors.

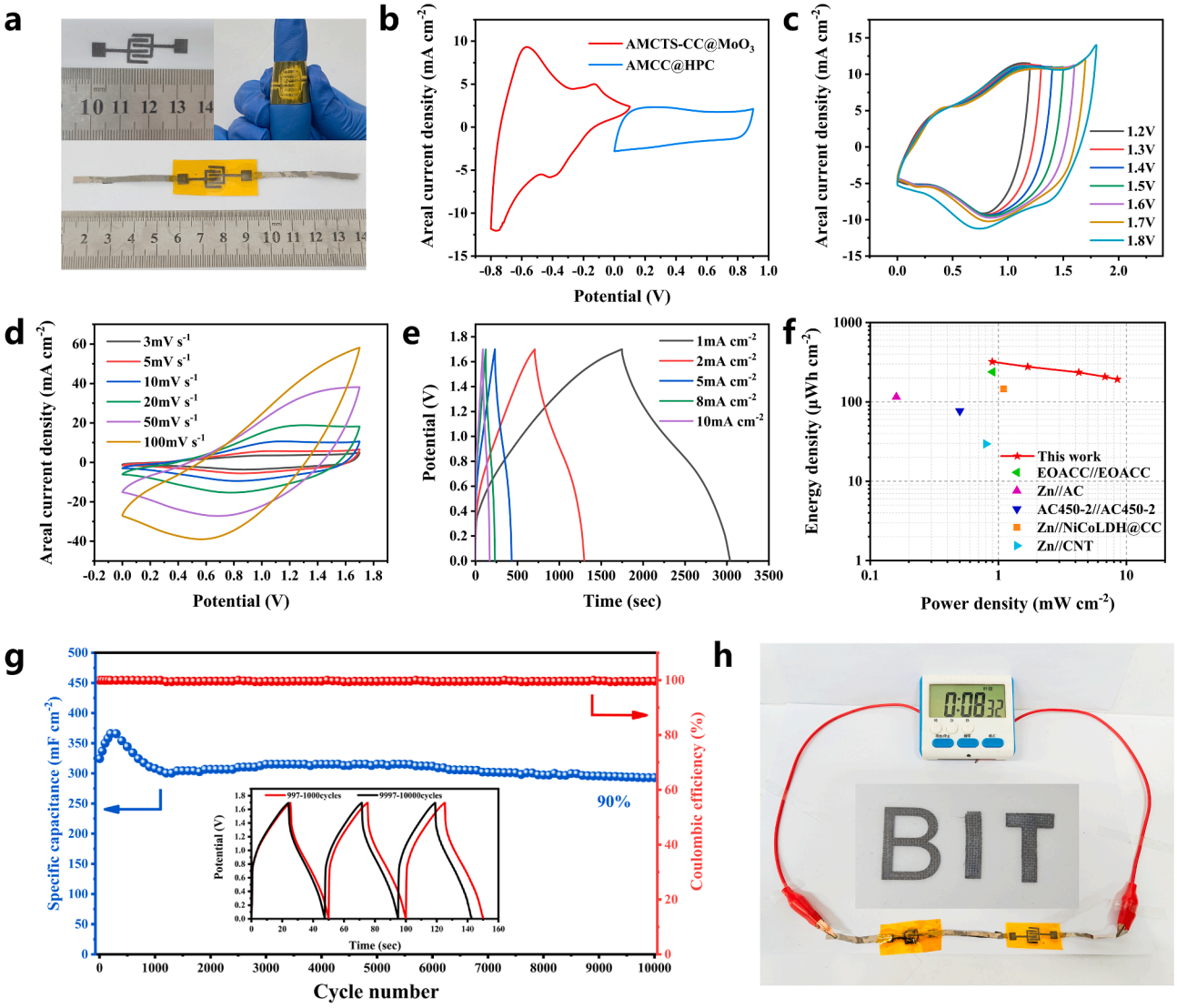


**Fig. 5.** Electrochemical performance of the assembled ZIMC. a) Digital photographs of the interdigitated electrode and an individual ZIMC with a bending shape. b) CV curves (10 mV $s^{-1}$) for AMCTS-CC@$MoO_3$, CC@N-HPC in PAM-2 M $ZnSO_4$; (c) CV curves at different potential window (10 mV $s^{-1}$); (d) CV curves with scan rates ranging from 3 to 100 mV $s^{-1}$; (e) GCD curves at various current densities from 1 to 10 mA $cm^{-2}$; (f) Ragone plots; (g) Cycling stability over 10,000 cycles at 20 mA $cm^{-2}$. h) A demonstration of ZIMC powering a timer.

## 3. Conclusion

To summarize, we propose an efficient and ultrafast air-assisted transient microwave-induced carbon thermal shock strategy for synthesizing molybdenum trioxide ($MoO_3$) on conductive carbon cloth within seconds. This method also facilitates the rapid introduction of defects and oxygen-containing functional groups on the flexible carbon substrate. Unlike traditional approaches involving multi-step reaction sequences characterized by constrained chemical kinetics, elevated energy consumption, and prolonged durations, the air-assisted transient microwave-induced carbon thermal shock process offers an exceptionally rapid heating rate, facilitating an ultrafast one-step reaction. The exceptionally Low reaction energy barriers and superior Gibbs free energy (ΔG) further substantiate the advantages of the microwave carbon thermal shock strategy over traditional synthesis methods in terms of both kinetics and thermodynamics. This reduces energy consumption, saves time, and promotes the formation of ultrafine nanoparticles, potentially achieving high electrochemical performance. Experimental assessments demonstrate that the prepared AMCTS-CC@$MoO_3$ exhibits outstanding electrochemical performance, reaching a notable areal capacitance of 2300 mF $cm^{-2}$ at an areal current density of 1 mA $cm^{-2}$, accompanied by remarkable cyclic stability. Furthermore, by utilizing AMCTS-CC@$MoO_3$ as the anode and CC@N-HPC as the cathode, a flexible zinc-ion micro supercapacitor (ZIMC) device achieves a notable areal energy density of 321 μWh $cm^{-2}$ alongside a stable operating voltage of 1.7 V. Additionally, this fabricated microdevice displays excellent long-term durability, withstanding 10,000 cycles while maintaining a high capacity retention rate of 90 %. Our research findings provide a promising pathway for the synthesis of high-performance anode materials for energy storage applications.

## CRediT authorship contribution statement

**Penghao Chai:** Writing – original draft, Software, Investigation, Data curation. **Yuchen Li:** Visualization, Data curation. **Qiulong Guan:** Supervision. **Jianghuan Li:** Data curation. **Lijie Li:** Software, Data curation. **Lixia Bao:** Software, Data curation. **Jiong Peng:** Supervision, Resources, Funding acquisition, Conceptualization. **Xin Li:** Writing – review & editing, Funding acquisition.

## Declaration of competing interest

The authors declare that they have no known competing financial interests or personal relationships that could have appeared to influence the work reported in this paper.

## Data availability

Data will be made available on request.

## Acknowledgments

This work was supported by Beijing Natural Science Foundation (No.2202050) and the National Natural Science Foundation of China (No. 21111120074). The characterization data were provided by Analysis & Testing Center of Beijing Institute of Technology.

## Appendix A. Supplementary data

Supplementary data to this article can be found online at https://doi.org/10.1016/j.cej.2024.151594.

## References

[1] L. Zhu, H. Xie, W. Zheng, K. Zhang, Multi-component solid PVDF-HFP/PPC/LLTO-nanorods composite electrolyte enabling advanced solid-state lithium metal batteries, Electrochimica Acta 435 (2022), https://doi.org/10.1016/j.electacta.2022.141384.
[2] J. Li, W. Zheng, L. Zhu, H. Zhou, K. Zhang, Incorporating lithium magnesium silicate into PVDF-HFP based solid electrolyte to achieve advanced solid-state lithium-ion batteries, Journal of Alloys and Compounds 960 (2023), https://doi.org/10.1016/j.jallcom.2023.170640.
[3] Y. Zheng, W. Zhao, D. Jia, Y. Liu, L. Cui, D. Wei, R. Zheng, J. Liu, Porous carbon prepared via combustion and acid treatment as flexible zinc-ion capacitor electrode material, Chem. Eng. J. 387 (2020), https://doi.org/10.1016/j.cej.2020.124161.
[4] Y. Liu, L. Wu, Recent advances of cathode materials for zinc-ion hybrid capacitors, Nano Energy 109 (2023), https://doi.org/10.1016/j.nanoen.2023.108290.
[5] H. Tang, J. Yao, Y. Zhu, Recent Developments and Future Prospects for Zinc-Ion Hybrid Capacitors: a Review, Adv. Energy Mater. 11 (14) (2021), https://doi.org/10.1002/aenm.202003994.
[6] Y. Wang, S. Sun, X. Wu, H. Liang, W. Zhang, Status and Opportunities of Zinc Ion Hybrid Capacitors: Focus on Carbon Materials, Current Collectors, and Separators, Nano-Micro Lett. 15 (1) (2023), https://doi.org/10.1007/s40820-023-01065-x.
[7] A. Amiri, E.N. Swart, A.A. Polycarpou, Recent advances in electrochemically-efficient materials for zinc-ion hybrid supercapacitors, Renewable Sustainable Energy Rev. 148 (2021), https://doi.org/10.1016/j.rser.2021.111288.
[8] S. Liu, C. Xu, H. Yang, G. Qian, S. Hua, J. Liu, X. Zheng, X. Lu, Atomic Modulation Triggering Improved Performance of MoO3 Nanobelts for Fiber-Shaped Supercapacitors, Small 16 (6) (2020), https://doi.org/10.1002/smll.201905778.
[9] Y. Zuo, K. Wang, P. Pei, M. Wei, X. Liu, Y. Xiao, P. Zhang, Zinc dendrite growth and inhibition strategies, Materials Today Energy 20 (2021), https://doi.org/10.1016/j.mtener.2021.100692.
[10] W. Zheng, H. Xie, L. Zhu, H. Zhou, K. Zhang, Elaborate artificial construction of porous biomass carbon interfacial layer on the surface of zinc anode toward high performance aqueous zinc-ion batteries, Journal of Energy Storage 76 (2024), https://doi.org/10.1016/j.est.2023.109808.
[11] C. Wang, X. Zeng, P.J. Cullen, Z. Pei, The rise of flexible zinc-ion hybrid capacitors: advances, challenges, and outlooks, J. Mater. Chem. A 9 (35) (2021) 19054–19082, https://doi.org/10.1039/d1ta02775a.
[12] H. Farsi, F. Gobal, H. Raissi, S. Moghiminia, On the pseudocapacitive behavior of nanostructured molybdenum oxide, J. Solid State Electrochem. 14 (4) (2009) 643–650, https://doi.org/10.1007/s10008-009-0830-5.
[13] X. Hou, M. Ruan, L. Zhou, J. Wu, B. Meng, W. Huang, K. Zhong, K. Yang, Z. Fang, K. Xie, Superior lithium storage performance in MoO3 by synergistic effects: Oxygen vacancies and nanostructures, J. Energy Chem. 78 (2023) 91–101, https://doi.org/10.1016/j.jechem.2022.11.011.
[14] J. Shi, Y. Hou, Z. Liu, Y. Zheng, L. Wen, J. Su, L. Li, N. Liu, Z. Zhang, Y. Gao, The high-performance MoO3−x/MXene cathodes for zinc-ion batteries based on oxygen vacancies and electrolyte engineering, Nano Energy 91 (2022), https://doi.org/10.1016/j.nanoen.2021.106651.
[15] B. Ahmed, M. Shahid, D.H. Nagaraju, D.H. Anjum, M.N. Hedhili, H.N. Alshareef, Surface Passivation of MoO3 Nanorods by Atomic Layer Deposition toward High Rate Durable Li Ion Battery Anodes, ACS Applied Materials & Interfaces 7 (24) (2015) 13154–13163, https://doi.org/10.1021/acsami.5b03395.
[16] S. Hariharan, K. Saravanan, P. Balaya, α-MoO3: A high performance anode material for sodium-ion batteries, Electrochemistry Communications 31 (2013) 5–9, https://doi.org/10.1016/j.elecom.2013.02.020.
[17] Y. Liu, J. Wang, Y. Zeng, J. Liu, X. Liu, X. Lu, Interfacial Engineering Coupled Valence Tuning of MoO3 Cathode for High-Capacity and High-Rate Fiber-Shaped Zinc-Ion Batteries, Small 16 (11) (2020), https://doi.org/10.1002/smll.201907458.
[18] S.R. Sahu, V.R. Rikka, P. Haridoss, A. Chatterjee, R. Gopalan, R. Prakash, A Novel α-MoO3/Single-Walled Carbon Nanohorns Composite as High-Performance Anode Material for Fast-Charging Lithium-Ion Battery, Adv. Energy Mater. 10 (36) (2020), https://doi.org/10.1002/aenm.202001627.
[19] Y. Zhang, P. Chen, Q. Wang, Q. Wang, K. Zhu, K. Ye, G. Wang, D. Cao, J. Yan, Q. Zhang, High-Capacity and Kinetically Accelerated Lithium Storage in MoO3 Enabled by Oxygen Vacancies and Heterostructure, Adv. Energy Mater. 11 (31) (2021), https://doi.org/10.1002/aenm.202101712.
[20] G. Saeed, S. Kumar, N.H. Kim, J.H. Lee, Fabrication of 3D graphene-CNTs/α-MoO3 hybrid film as an advance electrode material for asymmetric supercapacitor with excellent energy density and cycling life, Chem. Eng. J. 352 (2018) 268–276, https://doi.org/10.1016/j.cej.2018.07.026.
[21] W. Liu, J. Hao, C. Xu, J. Mou, L. Dong, F. Jiang, Z. Kang, J. Wu, B. Jiang, F. Kang, Investigation of zinc ion storage of transition metal oxides, sulfides, and borides in zinc ion battery systems, Chem. Commun. 53 (51) (2017) 6872–6874, https://doi.org/10.1039/c7cc01064h.
[22] N. Zhao, H. Fan, M. Zhang, J. Ma, Z. Du, B. Yan, H. Li, X. Jiang, Simple electrodeposition of MoO3 film on carbon cloth for high-performance aqueous symmetric supercapacitors, Chem. Eng. J. 390 (2020), https://doi.org/10.1016/j.cej.2020.124477.
[23] D. Gueon, T. Kim, J. Lee, J.H. Moon, Exploring the Janus structure to improve kinetics in sulfur conversion of Li-S batteries, Nano Energy 95 (2022), https://doi.org/10.1016/j.nanoen.2022.106980Adv Mater.
[24] B. Kaur, D. Maity, P.Y. Naidu, M. Deepa, Photo-rechargeable battery with an energetically aligned beetroot Dye/Cl-Graphene quantum dots/MoO3 nanorods composite, Chem. Eng. J. 468 (2023), https://doi.org/10.1016/j.cej.2023.143835.
[25] X. Wang, S. Huang, K. Guo, Y. Min, Q. Xu, Directed and Continuous Interfacial Channels for Optimized Ion Transport in Solid-State Electrolytes, Adv. Funct. Mater. 32 (49) (2022), https://doi.org/10.1002/adfm.202206976.
[26] W. Xu, K. Zhao, X. Liao, C. Sun, K. He, Y. Yuan, W. Ren, J. Li, T. Li, C. Yang, H. Cheng, Q. Sun, I. Manke, X. Lu, J. Lu, Proton Storage in Metallic H1.75MoO3 Nanobelts through the Grotthuss Mechanism, J. Am. Chem. Soc. 144 (38) (2022) 17407–17415, https://doi.org/10.1021/jacs.2c03844.
[27] Z. Qin, Y. Song, Y. Liu, X.-X. Liu, Aqueous calcium-ion storage in amorphous molybdenum oxide, Chem. Eng. J. 451 (2023), https://doi.org/10.1016/j.cej.2022.138681.
[28] S. Santhosh, M. Mathankumar, S. Selva Chandrasekaran, A.K. Nanda Kumar, P. Murugan, B. Subramanian, Effect of Ablation Rate on the Microstructure and Electrochromic Properties of Pulsed-Laser-Deposited Molybdenum Oxide Thin Films, Langmuir 33 (1) (2016) 19–33, https://doi.org/10.1021/acs.langmuir.6b02940.
[29] N.C. Ou, X. Su, D.C. Bock, L. McElwee-White, Precursors for chemical vapor deposition of tungsten oxide and molybdenum oxide, Coord. Chem. Rev. 421 (2020), https://doi.org/10.1016/j.ccr.2020.213459.
[30] F. Ullah, T.K. Nguyen, C.T. Le, Y.S. Kim, Pulsed laser deposition assisted grown continuous monolayer MoSe2, CrystEngComm 18 (37) (2016) 6992–6996, https://doi.org/10.1039/c6ce01392a.
[31] Z. Su, W. Ren, H. Guo, X. Peng, X. Chen, C. Zhao, Ultrahigh Areal Capacity Hydrogen-Ion Batteries with MoO3 Loading Over 90 mg cm−2, Adv. Funct. Mater. 30 (46) (2020), https://doi.org/10.1002/adfm.202005477.
[32] C.M. Schaefer, J.M. Caicedo Roque, G. Sauthier, J. Bousquet, C. Hébert, J.R. Sperling, A. Pérez-Tomás, J. Santiso, E. del Corro, J.A. Garrido, Carbon Incorporation in MOCVD of MoS2 Thin Films Grown from an Organosulfide Precursor, Chem. Mater. 33(12) (2021) 4474-4487. https://doi.org/10.1021/acs.chemmater.1c00646.
[33] C. Wan, X. Duan, Microwave Shock Synthesis beyond Thermodynamic Equilibrium, Matter 1 (3) (2019) 555–557, https://doi.org/10.1016/j.matt.2019.08.006.
[34] S. Chen, L. Nie, X. Hu, Y. Zhang, Y. Zhang, Y. Yu, W. Liu, Ultrafast Sintering for Ceramic-Based All-Solid-State Lithium-Metal Batteries, Adv. Mater. 34 (33) (2022), https://doi.org/10.1002/adma.202200430.
[35] J. Wan, L. Huang, J. Wu, L. Xiong, Z. Hu, H. Yu, T. Li, J. Zhou, Microwave Combustion for Rapidly Synthesizing Pore-Size-Controllable Porous Graphene, Adv. Funct. Mater. 28 (22) (2018), https://doi.org/10.1002/adfm.201800382.
[36] R. Kumar, C. Liu, G.-S. Ha, K.H. Kim, S. Chakrabortty, S.K. Tripathy, Y.-K. Park, M. A. Khan, K.K. Yadav, M.M.S. Cabral-Pinto, B.-H. Jeon, A novel membrane-integrated sustainable technology for downstream recovery of molybdenum from industrial wastewater, Resour, Conserv. Recycl. 196 (2023), https://doi.org/10.1016/j.resconrec.2023.107035.
[37] Y. Qiao, S. Xu, Y. Liu, J. Dai, H. Xie, Y. Yao, X. Mu, C. Chen, D.J. Kline, E.M. Hitz, B. Liu, J. Song, P. He, M.R. Zachariah, L. Hu, Transient, in situ synthesis of ultrafine ruthenium nanoparticles for a high-rate Li–CO2 battery, Energy Environ. Sci. 12 (3) (2019) 1100–1107, https://doi.org/10.1039/c8ee03506g.
[38] S. Wang, W. Hua, A. Missyul, M.S.D. Darma, A. Tayal, S. Indris, H. Ehrenberg, L. Liu, M. Knapp, Kinetic Control of Long-Range Cationic Ordering in the Synthesis of Layered Ni-Rich Oxides, Adv. Funct. Mater. 31 (19) (2021), https://doi.org/10.1002/adfm.202009949.
[39] W. Huang, K. Zhang, B. Yuan, L. Yang, M. Zhu, Predominant intercalation of H+ enables ultrahigh rate capability of oxygen deficient MoO3 for aqueous Al-ion batteries, Energy Storage Mater. 50 (2022) 152–160, https://doi.org/10.1016/j.ensm.2022.05.016.
[40] T. Xiong, Y. Zhang, Y. Wang, W.S.V. Lee, J. Xue, Hexagonal MoO3 as a zinc intercalation anode towards zinc metal-free zinc-ion batteries, J. Mater. Chem. A 8 (18) (2020) 9006–9012, https://doi.org/10.1039/d0ta02236e.

[41] X.-H. Yang, Y.-F. Zuo, P.-F. Feng, N. Wang, J. Li, Y.-Q. Wang, G.-H. Zhang, K.-C. Chou, Mechanism and kinetics of decomposition reaction of ultrafine ammonium molybdate for preparing ultrafine MoO3 powder, Mater. Chem. Phys. 302 (2023), https://doi.org/10.1016/j.matchemphys.2023.127760.
[42] T.N. Kovács, D. Hunyadi, A.L.A. de Lucena, I.M. Szilágyi, Thermal decomposition of ammonium molybdates, J. Therm. Anal. Calorim. 124 (2) (2016) 1013–1021, https://doi.org/10.1007/s10973-015-5201-0.
[43] M.-S. Balogun, W. Qiu, F. Lyu, Y. Luo, H. Meng, J. Li, W. Mai, L. Mai, Y. Tong, All-flexible lithium ion battery based on thermally-etched porous carbon cloth anode and cathode, Nano Energy 26 (2016) 446–455, https://doi.org/10.1016/j.nanoen.2016.05.017.
[44] D. Guo, J. Qin, Z. Yin, J. Bai, Y.-K. Sun, M. Cao, Achieving high mass loading of Na3V2(PO4)3@carbon on carbon cloth by constructing three-dimensional network between carbon fibers for ultralong cycle-life and ultrahigh rate sodium-ion batteries, Nano Energy 45 (2018) 136–147, https://doi.org/10.1016/j.nanoen.2017.12.038.
[45] T. Li, M. Beidaghi, X. Xiao, L. Huang, Z. Hu, W. Sun, X. Chen, Y. Gogotsi, J. Zhou, Ethanol reduced molybdenum trioxide for Li-ion capacitors, Nano Energy 26 (2016) 100–107, https://doi.org/10.1016/j.nanoen.2016.05.004.
[46] Z. Liu, Z. Zhao, Y. Wang, S. Dou, D. Yan, D. Liu, Z. Xia, S. Wang, In Situ Exfoliated, Edge-Rich, Oxygen-Functionalized Graphene from Carbon Fibers for Oxygen Electrocatalysis, Adv. Mater. 29 (18) (2017), https://doi.org/10.1002/adma.201606207.
[47] X. Xiao, T. Li, Z. Peng, H. Jin, Q. Zhong, Q. Hu, B. Yao, Q. Luo, C. Zhang, L. Gong, J. Chen, Y. Gogotsi, J. Zhou, Freestanding functionalized carbon nanotube-based electrode for solid-state asymmetric supercapacitors, Nano Energy 6 (2014) 1–9, https://doi.org/10.1016/j.nanoen.2014.02.014.
[48] X. Li, F. Chen, B. Zhao, S. Zhang, X. Zheng, Y. Wang, X. Jin, C. Dai, J. Wang, J. Xie, Z. Zhang, Y. Zhao, Ultrafast Synthesis of Metal-Layered Hydroxides in a Dozen Seconds for High-Performance Aqueous Zn (Micro-) Battery, Nano-Micro Lett. 15 (1) (2023), https://doi.org/10.1007/s40820-022-01004-2.
[49] H. Siddiqui, N. Singh, P. Naidu, K. Bhavani Srinivas Rao, S. Gupta, A. Kumar Srivastava, M.S. Santosh, S. Natarajan, S. Kumar, L.F. Dumée, S. Rtimi, Emerging electrochemical additive manufacturing technology for advanced materials: Structures and applications, Mater. Today 70 (2023) 161–192, https://doi.org/10.1016/j.mattod.2023.10.008.
[50] Y. Sun, Y.-Z. Li, M. Yuan, Requirements, challenges, and novel ideas for wearables on power supply and energy harvesting, Nano Energy 115 (2023), https://doi.org/10.1016/j.nanoen.2023.108715.